colloids and interfaces

MDPI

Article

Particulate Cake Formation and Pressure Development in Microfluidic Membrane Filters

Md Mohaimeen Ul Islam [1], Md Abdul Karim Miah [1], Michael G. Olsen [1] and Jaime J. Juárez [1,2,*]

[1] Department of Mechanical Engineering, Iowa State University, Ames, IA 50011, USA; mohaimen@iastate.edu (M.M.U.I.); mgolsen@iastate.edu (M.G.O.)
[2] Center for Multiphase Flow Research and Education, Iowa State University, Ames, IA 50011, USA
* Correspondence: jjuarez@iastate.edu; Tel.: +1-515-294-3298

Abstract

In filtering applications, particulates build up on the filtering membrane, forming a cake layer that directly affects permeability and increases pressure across the filter. In this investigation, 10 μm microchannels were fabricated using photolithography to create filters with porosities that vary between 9% and 23%. To estimate cake layer growth, a water–glycerol solution containing a 1% volume fraction of 15 μm polystyrene particles was injected by a syringe pump into filtration media at 300, 500 and 700 μL h^{-1} flow rates for 300 s. A differential pressure sensor was mounted across the inlet and outlet channels to measure transmembrane pressure (TMP) over time. It was found that higher flow rates accelerate particle deposition on the membrane surface, which contributes to a larger cake area and a corresponding rise in TMP. These findings will give valuable insights into clogging dynamics to optimize the filter's efficiency and lifespan.

Keywords: microfiltration; cake formation; transmembrane pressure; cake porosity

1. Introduction

Microfluidic filtration is utilized in a variety of applications, including medical diagnostics [1–3], water treatment [4–6], pollution mitigation [7,8], and high-throughput particle separation [9–11]. Microfluidic devices designed for filtration typically use membranes as a filtering mechanism due to their simplicity and ease of fabrication [12–14]. These devices rely on hydrodynamic principles (e.g., fluid velocity, pressure drop, viscosity) to process particle-laden samples [15,16] and are typically applied to particle sizes ranging on the order of 0.1 to 10 μm [17]. During the microfiltration process, particles accumulate at the filtering membrane pore entrance due to sieving, bridging, or aggregation [18,19]. The layer of particles deposited on the membrane as a result of this process is known as a cake layer [20]. The cake layer contributes to membrane clogging and hydraulic resistance, which are responsible for fouling [18,19,21].

Clogging dynamics represent an important phenomenon that is governed by a complex interplay of particle transport, deposition, and compaction mechanisms evolving over time and space. Particle–surface interactions can lead to different modes of fouling depending on surface properties [22]. Hydrophilic surface interactions lead to the creation of dendritic particle structures that offer lower resistance to the passage of fluid than hydrophobic structures, which arch across channel pores and lead to rapid fouling conditions. Filter geometry and pore arrangement directly influence the local flow field and particle trajectories near the filtration interface, affecting the location and rate of particle deposition. Previous studies

Check for updates

Academic Editors: Reinhard Miller and Aliyar Javadi

Received: 18 August 2026
Revised: 13 October 2026
Accepted: 23 October 2026
Published: 28 October 2026

Copyright: © 2026 by the authors. Licensee MDPI, Basel, Switzerland. This article is an open access article distributed under the terms and conditions of the Creative Commons Attribution (CC BY) license.

have shown that membrane pore geometry and pore spacing can significantly alter the initial fouling behavior and the organization of the first deposited particle layer [23]. Additionally, operating conditions such as flow rate and transmembrane pressure determine the balance of hydrodynamic forces acting on suspended particles and consequently influence particle capture, detachment, and cake growth [24,25]. As deposition progresses, the spatial arrangement, porosity, and compactness of the cake layer govern its permeability and specific hydraulic resistance; consequently, variations in cake microstructure can produce substantially different hydraulic resistances and filtration behaviors [26].

In microfluidic systems, microchannel array structures and pillar formations may act as a scale-up model for membrane pore structures, where particle deposition, layer formation, inner particle rearrangement, and TMP development can be monitored directly [27–29]. The ability to precisely control pore geometry, spacing, and effective porosity, coupled with high-speed imaging, allows researchers to isolate and quantify the effects of individual parameters on fouling mechanisms. Moreover, microfluidic observations can be directly coupled with computational fluid dynamics–discrete element method (CFD-DEM) simulations to validate pore-scale force balances (permeation drag, lift, particle–particle interactions) and refine mechanistic models [13,16,30]. These capabilities position microfluidic systems as an essential tool for investigating cake dynamics and clogging behavior in microfiltration applications.

Despite these advances, there is a lack of systematic experimental datasets that concurrently vary flow rate, filter porosity, and operating duration to produce quantitative maps of the cake growth rate, TMP development, and cake porosity evolution [31]. Existing studies provided valuable insight into membrane fouling [30,32,33]. However, the coupled relationships among the filter geometry, flow conditions, particle deposition behavior, cake layer growth, pressure dynamics, and cake microstructure remain insufficiently connected in a systematic experimental framework. The early stages of filtration processes, distinguished by fluctuations in resistance and spatial heterogeneity, are not yet well understood over a range of operating conditions [26,33]. Furthermore, while pore-scale models have advanced considerably, systematic validation across a broad range of microfluidic geometries and particle systems is still needed to link flow, porosity, and cake structure. Moreover, TMP measurements would enable the rational selection of pore geometry and operating conditions to maximize flux while minimizing cleaning frequency and avoiding irreversible cake consolidation [34].

In the experiments presented here, membrane microfilters with porosities of 9%, 12%, 17%, and 23% were fabricated using the photolithography technique. One-micron-diameter fluorescent tracer particles were used to conduct microscopic particle image velocimetry (μPIV) analysis to understand flow patterns and velocity fields around the microchannels. A model particle suspension consisting of 15 μm diameter polystyrene particles in a mixture of water and glycerol was filtered with 9, 12, 17 and 23% porous microfilters at flow rates of 300, 500, and 700 $\mu L\ h^{-1}$ over a period of 300 s to observe cake layer growth. Throughout this experiment, differential pressure sensors measured TMP. By systematically varying both filter porosity and flow rate, this work quantifies how geometric and hydrodynamic conditions jointly influence particle deposition rates, cake layer growth, pressure development, and the internal compaction state of the cake layer. The findings provide underlying insights into the trade-offs between rapid cake growth and particle packing density, offering valuable guidance for the design and operation of membrane filtration systems to enhance efficiency and extend operational life.

2. Materials and Methods

2.1. Microfluidic Device Fabrication

The microchannel filtration device used in this work consisted of a main channel with dimensions of a 2 mm width and 24 mm length. The filter section of the device features a series of walls of 1.97 mm in length and width (w), which vary. These walls have a spacing of 10 µm between each other. The wall widths (w) used in this work were 35 µm, 50 µm, 80 µm, and 100 µm to create filters with effective porosities of 23%, 17%, 12%, and 9%, respectively. The effective porosity was calculated as the ratio of the total open volume to the total volume of the filtering section. Reservoirs were incorporated into either end of the microchannel, each with a 4 mm diameter. Figure 1 shows a schematic representation of one of the microfilters.

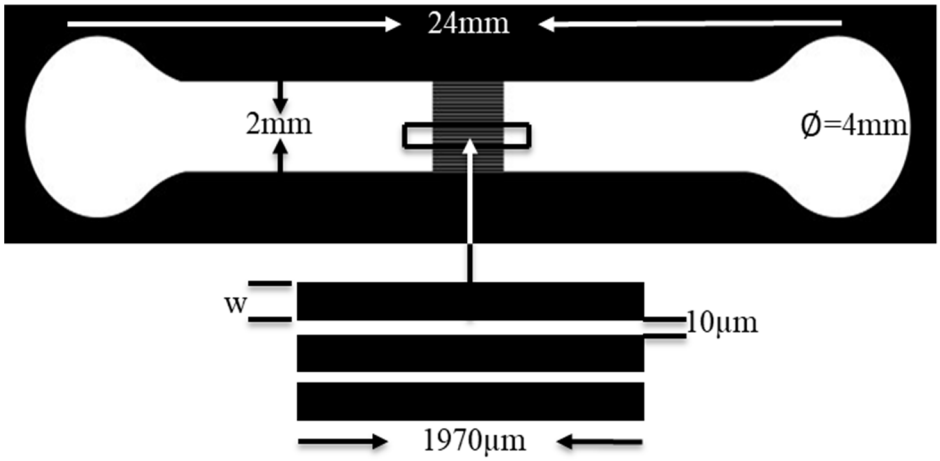


Figure 1. A representative image showing one of the microfilter designs used in this work. The widths of the walls in the center varied from 35 µm to 100 µm.

A mask was sourced from Fineline Imaging, Inc. (Colorado Springs, CO, USA) and was used to fabricate the microfilters with photolithography [35]. In this process, a negative photoresist (Kayaku Advanced Materials, Westborough, MA, USA, SU-8 2050) was spin-coated onto a 100 mm diameter silicon wafer (University Wafer, Boston, MA, USA, catalog # 452) to achieve a depth of 50 µm. The wafer was prebaked at 65 °C and 95 °C for three minutes and seven minutes, respectively, to remove bubbles and solvent before exposure to a UV light source. After exposing the wafer to a UV light source through a photomask, the wafer underwent a post-exposure baking treatment to stabilize the photoresist and reduce stress. The unexposed photoresist was rinsed away using SU-8 developer. Finally, the wafer was exposed to a final heating step at 150 °C for 10 min.

The wafer was placed in a 150 mm diameter Petri dish, and a silane (1H,1H,2H,2H-perfluorooctyl-trichlorosilane) vapor was applied for 6 h to promote polydimethylsiloxane (PDMS) demolding. PDMS was prepared by mixing Sylgard 184 (Dow, Midland, MI, USA, GMID 01673921) with a curing agent in a ratio of 10:1 and placed into a vacuum chamber to remove excess bubbles.

Once the bubbles were removed, PDMS was poured into the Petri dish and placed into an oven for 6 h at 42 °C to enhance crosslinking. After curing PDMS, the microfilter mold was cut out, and a biopsy punch was used to create holes in the reservoirs. A plasma chamber (Harrick Plasma, Ithaca, NY, USA, model no. PDC-32G) was used to bond the PDMS microchannel to 48 mm × 65 mm cover glass (Brain Research Laboratories, Waban, MA, USA, catalog no. 4865-1D) at the highest setting for 45 s. The device was then heated to 100 °C for 10 min. Finally, two 3/32" diameter silicone tubes (U.S. Plastic Corp., Lina,

OH, USA, 57286) were inserted into the reservoir holes and sealed with PDMS, as shown in Figure 2.

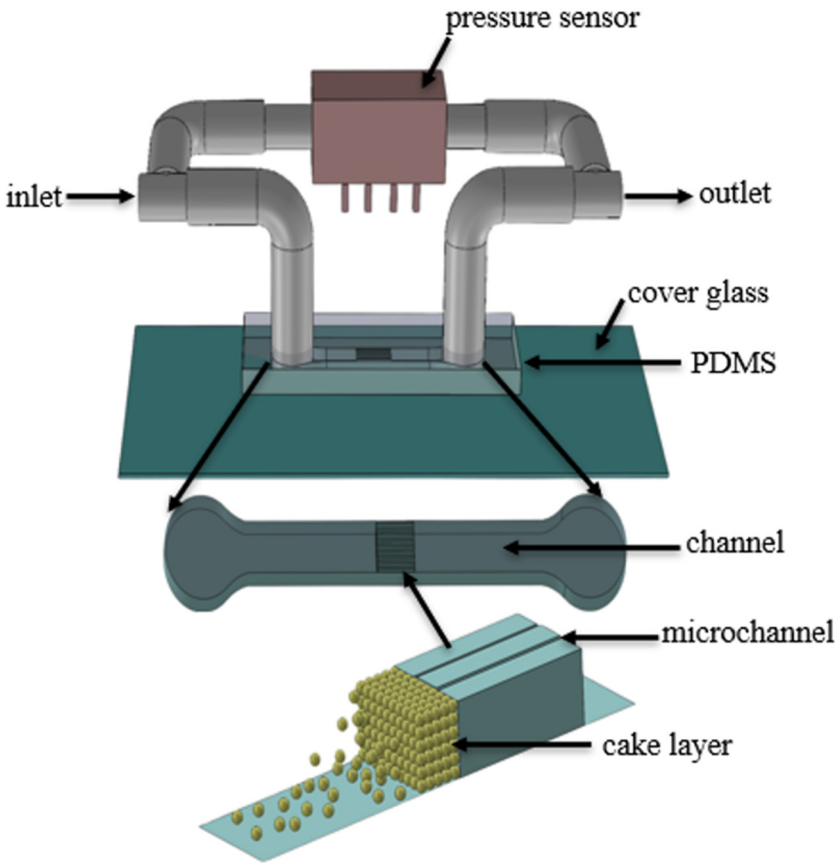


Figure 2. A schematic representation of the PDMS microchannel filter used in this experiment. (**Top**) A differential pressure sensor connects to the inlet and outlet of the microfilter to record the pressure drop in this system. (**Middle**) An overview of the microchannel filter showing its placement in the center. (**Bottom**) The filter section blocks the passage of colloidal particles, leading to the formation of a cake layer.

2.2. Sample Preparation

Two separate solutions were prepared for membrane filtration experiments. The first solution contained fluorescent 1 µm polystyrene particles (ThermoFisher Scientific, Waltham, MA, USA catalog # F8852), which were selected for microscopic particle image velocimetry (µPIV) experiments. This solution was prepared by mixing 500 µL of 1 µm diameter fluorescent particle stock solution per milliliter of 80.8% DI water and 19.2% glycerol (v/v). The Reynolds numbers ($\mathrm{Re} = \rho UD/\mu$), representing the ratio of inertial to viscous forces [36], were 0.196, 0.147, 0.104, and 0.077, inside the filter microchannels for 9, 12, 17, and 23% porosities, respectively, and 0.103 within the main channel at the highest flow rate (700 µL h^{-1}), indicating creeping flow conditions throughout the device. The corresponding Stokes number ($\mathrm{St} = \rho_p d_p^2 v/18\mu d_C$), which represents the particle response time with respect to the characteristic fluid time, was found to be 5.9×10^{-7} in the main channel and ranged from 3.8×10^{-5} to 1.5×10^{-5} inside the filter pores for the 9–23% porosity filters, respectively, indicating that the 1 µm particles will accurately trace the flow field [37]. The cake layer experiments employed 15 µm diameter polystyrene beads (Abvigen, Skillman, NJ, USA, catalog # ABPS-1500), which were also dispersed in 80.8% DI water and 19.2% glycerol (v/v) to achieve the neutral buoyancy of the particles [38].

2.3. Experimental Methods

The fluid was introduced to the microfilters through a syringe pump (Chemyx, Stafford, TX, USA, Model 740) at flow rates of 300, 500, and 700 µL h^{-1}, as shown in Figure 3. Before each experiment, the filters were tested to ensure that the flow passed through unimpeded and to remove any bubbles that might be present inside the microfilters. The observation was captured by an Olympus IX70 inverted microscope coupled with a high-speed camera (Photron, San Diego, CA, USA, Nova S6).

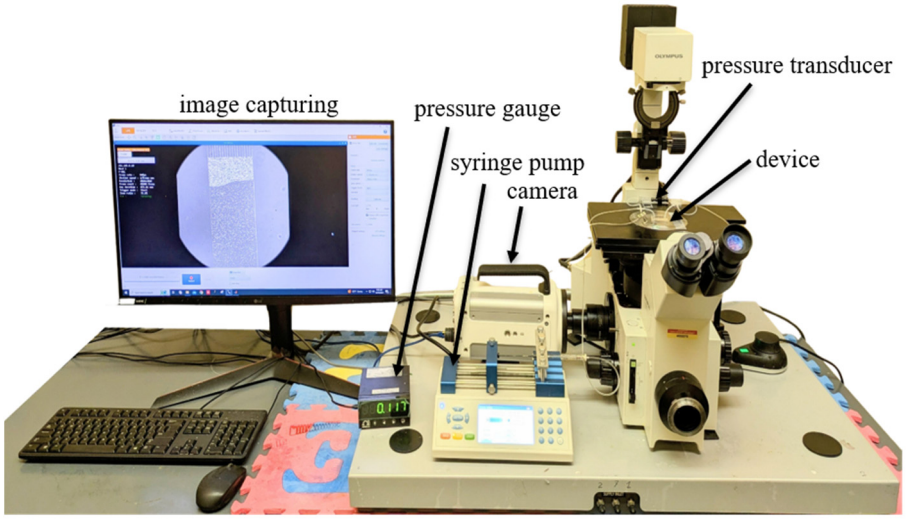


Figure 3. Experimental configuration for data acquisition in microfilters.

To visualize the velocity field using µPIV, 1 µm fluorescent particles were introduced as seed particles. The µPIV experiments were performed around a 10 µm pore (i.e., interior filtering microchannel), and images were recorded at 2000 fps using a 40× microscope objective lens. The captured images were analyzed and visualized using PIVLab-3.14 [39], an open-source software available for MATLAB-2026a. Each µPIV analysis was performed using ensemble correlation algorithms in PIVLab to extract local velocity information [40]. The in-plane spatial resolution of the vector map was calculated as 4.77 µm, while the out-of-plane resolution is 7.3 µm [41–44].

To investigate cake formation, a 15 µm particle solution was employed. A differential pressure sensor (Dwyer-Omega, Michigan City, IN, USA, PX26-005GV) was mounted across the reservoirs to record TMP using Platinum software-1.2.0.7 from Dwyer Omega. The introduction of the particles was paused momentarily as they approached the microchannel filter to allow the pressure to stabilize. Once the pressure was stable, the pump was restarted for 300 s. This approach allowed for the capture of particle deposition on the filter surface and recording associated changes in pressure. Since particle deposition is a stochastic process [45], we repeated each experiment in triplicate and averaged the resulting differential pressure and cake layer growth data. Images were recorded at 50 frames per second (fps) with a 4× objective lens to maximize the field of view. The images were used to measure the area encompassed by particles deposited on the microfilter in each image. The total area for each second interval was filtered and plotted to illustrate cake layer development. The binarized images also permitted the identification of void spaces within the cake layer as a metric to determine packing effectiveness at the flow conditions examined in this investigation.

2.4. Cake Layer Porosity Model

The total pressure drop through a microchannel filter with a depositing cake layer is [46]

$$\Delta P = \Delta P_m + \Delta P_{cl} \quad (1)$$

where ΔP_m is the pressure drop through the microchannel, and ΔP_{cl} is the cake layer pressure drop. The pressure drop through the microchannel can be calculated on the basis of hydraulic resistance as [47]

$$\Delta P_m = (R_c + R_f + R_c)Q \quad (2)$$

where R_c is the hydraulic resistance of the channel section, R_f is the hydraulic resistance of the filter section, and Q is the volumetric flow rate. The term R_c appears twice to account for channel sections upstream and downstream of the filter section. This term is assumed to be symmetric in this device. Hydraulic resistance depends on fluid properties and channel geometry, which may be expressed as [48]

$$R_c = \frac{12\mu L_c}{h^3 w_c}$$

$$R_f = \frac{12\mu L_f}{n h^3 w_f}$$

where μ is fluid viscosity, h is channel height, L_c is the length of the channel section, L_f is the length of the filter section, n is the number of channels that make up the filter section of our microfilter device, w_c is the width of the channel section, and w_f is the width of the filter section. The total length of our microchannel is expressed as $L = 2L_c + L_f$.

In the absence of particles, there is no cake layer, and thus one expects the differential pressure measurements to solely depend on channel geometry and fluid viscosity. Once the particle deposition process begins, the differential pressure measurement tracks ΔP_{cl} as a function of time. Cake layer pressure may be expressed by Darcy's law [49]

$$\Delta P_{cl} = \left(\frac{\mu L_{cl}}{K_{cl} A}\right) Q \quad (3)$$

where Q is the fluid flow rate, μ is the dynamic viscosity of the medium (~1.9 mPa-s for the water–glycerol mixture used in this work [50]), L_{cl} is the effective cake layer length at the time ΔP_{cl} is measured, $A = hw_c$ is the channel cross-sectional area (50 µm × 2000 µm), and K_{cl} is time-varying cake layer permeability. In this work, we define the effective cake layer length to be $L_{cl} = A_{cl}/w_c$, where A_{cl} is the cake layer area measured by ImageJ. The permeability of a cake layer composed of monodisperse spheres is given by the Kozeny–Carman equation [51]

$$K_{cl} = \frac{\varepsilon^3 d_m^2}{180(1-\varepsilon)^2} \quad (4)$$

where d_m is the mean particle diameter, and ε is cake layer porosity. Substituting Equation (4) into Equation (3) yields

$$\Delta P_{cl} = \left[\frac{180\mu L_{cl}(1-\varepsilon)^2}{A d_m^2 \varepsilon^3}\right] Q \quad (5)$$

Equation (5) can be rearranged to yield a polynomial

$$\left(\frac{d_m^2}{180}\right)\left[\frac{A\Delta P_{cl}}{\mu L_{cl} Q}\right]\varepsilon^3 - \varepsilon^2 + 2\varepsilon - 1 = 0$$

The roots of this can be evaluated using a numerical software package (e.g., MATLAB-2026a) to find cake layer porosity at any point in time using measurements of DP_{cl}.

3. Results and Discussion

3.1. Velocity Field Analysis

The velocity flow field was determined in a 9% porosity filter using μPIV analysis, as described in Section 2.3. Each pore section was fixed at a width of 10 μm and a height of 50 μm. Figure 4 shows the flow field upstream and downstream around a single 10 μm membrane pore. Within the main channel, we anticipate that the average flow velocity is $u_{avg} = Q/A$ [36]. The average flow velocity within the pore, based on mass conservation [52], is $u_{avg,p} = Q/A\varepsilon_p$, where ε_p is the filter porosity. The experimentally measured bulk velocities (0.763 mm/s, 1.26 mm/s, and 1.77 mm/s for 300 μL h^{-1}, 500 μL h^{-1}, and 700 μL h^{-1}, respectively) showed excellent agreement with theoretical values (0.833 mm/s, 1.39 mm/s, and 1.94 mm/s), with deviations of 9–10%. Similarly, the average velocities within the pore (10.20, 16.16, and 22.80 mm/s) closely matched theoretical predictions (9.3, 15.5, and 21.7 mm/s), validating the mass conservation principle across the pore constriction [53,54]. This level of agreement is consistent with recent validation studies in hyperbolic contractions, where experimental μPIV velocity fields matched CFD predictions within errors smaller than 10% [55]. The slight discrepancies between experiment and theory can be attributed to PIV measurement uncertainty, the finite spatial resolution of the PIV technique (~5 μm), and three-dimensional flow effects in the actual geometry that are not captured in the 2D measurement plane [41,56].

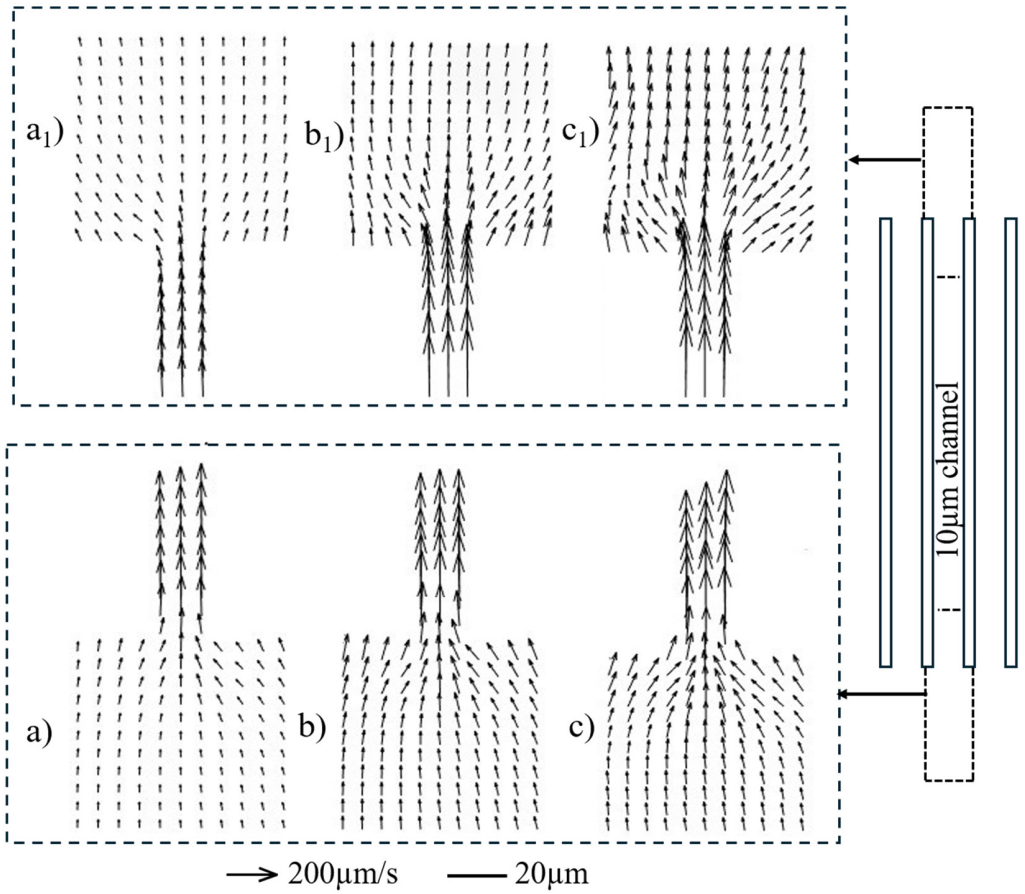


Figure 4. μPIV velocity vector fields at the entrance and exit of the 10 μm channel at flow rates of 300 μL h^{-1} (**a**,**a**$_1$), 500 μL h^{-1} (**b**,**b**$_1$), and 700 μL h^{-1} (**c**,**c**$_1$). The lower panels show the entrance flow field, while the upper panels show the exit flow field. The 20 μm bar indicates the spatial scale, and the 200 μm s^{-1} arrow represents the velocity vector scale.

At the pore entrance (Figure 4a–c), the flow field undergoes dramatic changes in velocity, magnitude and direction. The velocity vectors showed significant convergence as the fluid approached the 10 μm pore constriction, with the streamlines converging toward the pore centerline [57]. This convergent flow pattern intensified at higher flow rates, with vectors at 700 μL h^{-1} (Figure 4c) showing more pronounced lateral velocity components compared to 300 μL h^{-1} (Figure 4a). This velocity acceleration generates substantial hydrodynamic forces that influence not only initial particle deposition but also the subsequent cake layer structure. In Section 3.3, the cake structure porosity is discussed, where at lower flow rates (300 μL h^{-1}), particles arrive with lower kinetic energy and experience moderate hydrodynamic forces, allowing time for rearrangement into denser packing configurations. However, at the highest flow rate (700 μL h^{-1}), the elevated particle flux and increased local shear/strain rates promote kinetically trapped cake structures. When deposition occurs more rapidly than particles can rearrange and consolidate, non-equilibrium configurations can be locked in, which leads to looser packing and higher porosity [30,33]. This mechanism is consistent with our observations and explains the counterintuitive finding that higher flow rates produce both higher TMP and higher cake porosity.

Upon exiting the 10 μm pore constriction into the main channel, the flow rapidly expanded and decelerated. The velocity vectors exhibited a diverging pattern as the high-velocity jet emerging from the pore spread laterally to fill the larger cross-sectional area [58]. At all three flow rates, the downstream region (Figure 4a_1–c_1) exhibited central high velocity surrounded by regions of lower velocity. This jet structure was pronounced immediately downstream of the pore exit and gradually dissipated as flow progressed downstream. The velocity magnitude decreased as the flow redistributed across the channel width, eventually recovering toward a uniform profile further downstream [59].

3.2. Cake Layer Area vs. Pressure Drop

For the cake layer experiments, 15 μm diameter polystyrene particles were dispersed as described in the Materials and Methods. This particle dispersion was passed into the microchannel for 300 s. The 10 μm pores in the filter section allowed the filtrate to pass through while particles aggregated on the filter surface. Cake layer formation was captured via optical video microscopy at a rate of 50 fps. Images from these experiments are shown in Figure 5. Generally, the aggregation rate driving cake layer formation was found to increase with flow rate. This is consistent with a mass flux of $J \approx \phi u_{avg}$, where ϕ is the particle volume fraction [60].

Figure 6 shows the measured cake layer area as a function of time. After a period of 300 s, the area measured in the experiments for the 300 μL h^{-1} flow rate varied between 2.5 mm^2 for 9% porosity and 3.3 mm^2 for 23% porosity, with a mean deposition area of 3.01 ± 0.38 mm^2 across all filter porosities. Increasing the flow rate to 500 μL h^{-1} or 700 μL h^{-1} increased the mean deposition area to 5.11 ± 0.87 mm^2 and 6.47 ± 0.57 mm^2, respectively. A regression analysis shows that the *p*-values for flow rate and porosity were found to be 1.6×10^{-5} and 0.34, respectively. This suggests that porosity has no statistically significant impact on cake layer area (i.e., *p*-value must be less than 0.05 for statistical significance). Using the flow rate as an independent variable, we find that

$$A_{cake} \approx \left(0.0096 \frac{mm^2 \cdot hr}{\mu L}\right) Q$$

with a coefficient of determination of 0.84. As stated above, this is consistent with the mass flux of $J \approx \phi u_{avg}$, where $u_{avg} = Q/A$. Hence, we expect a proportional relationship between the growth of the cake layer and the flow rate.

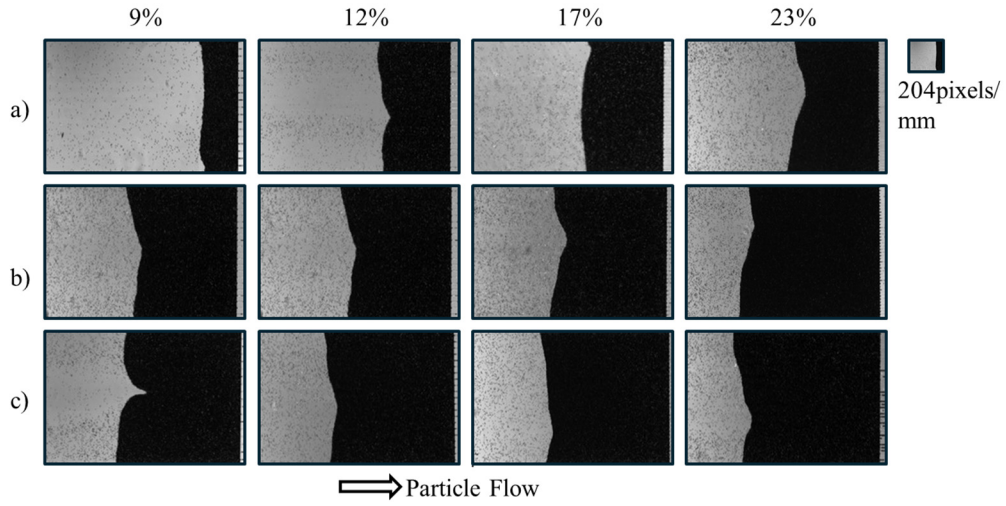


Figure 5. Particle deposition on the filtering membrane after 300 s. The black area represents the cake, and the particle transportation is visible in the gray sections. Each column represents a distinct porous filter, highlighting the effect of filter porosity at flow rates of (**a**) 300 μL h^{-1}, (**b**) 500 μL h^{-1} and (**c**) 700 μL h^{-1}.

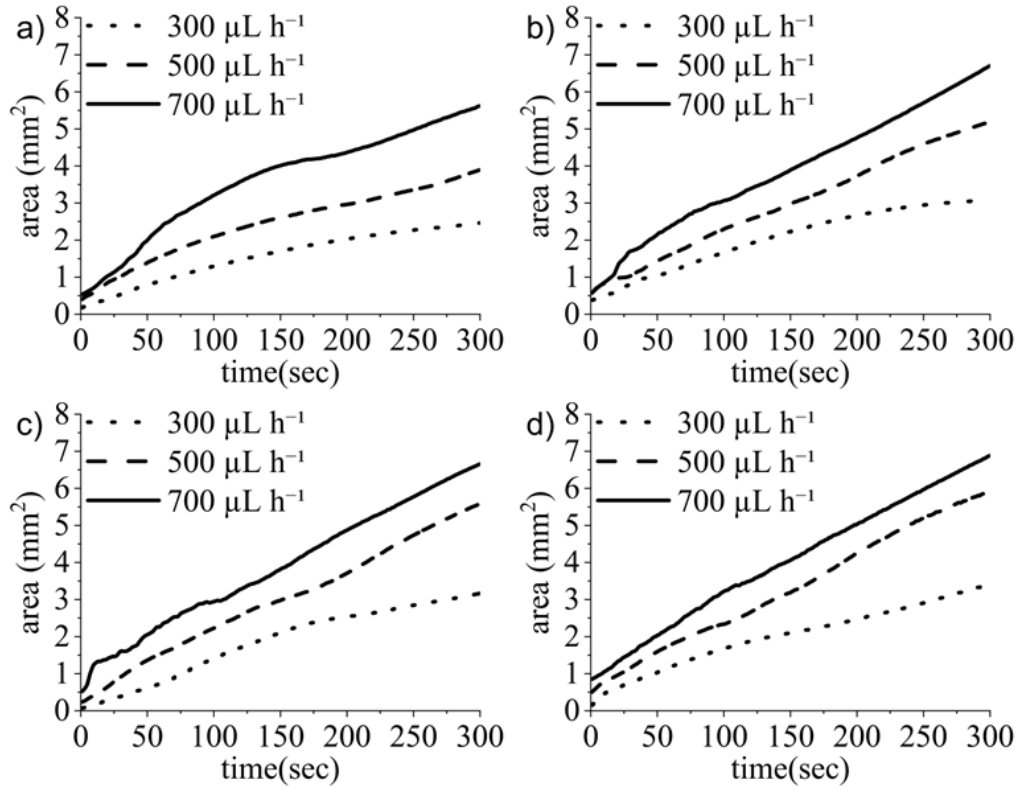


Figure 6. Cake layer growth over a 300 s filtration period at different flow rates for filters with porosities of (**a**) 9%, (**b**) 12%, (**c**) 17%, and (**d**) 23%.

In addition, as particle concentration and filtration were kept constant in this study, the total amount of suspension delivered to the filter increased directly with flow rate. Therefore, over the 300 s filtration period, the total suspension volume was higher at 700 μL h^{-1} than at 300 μL h^{-1}. Thus, the larger cake area observed at higher flow rates reflects both the greater particle supply to the filter and the influence of the local hydrodynamic conditions that we observed in μPIV analysis.

The cake layer growth experiments also simultaneously monitored TMP. Initially, there was only clean filter resistance, and eventually, when particles began to deposit on the membrane surface, they created a blockage, adding further hydraulic resistance to the fluid flow [52,61]. The μPIV measurements showed that the flow accelerated as it approached the pore, with the highest local velocities occurring near the 10 μm constriction, while lower velocities were observed farther from the filtration surface. This pore-scale acceleration indicates stronger convective transport toward the membrane and causes rapid particle deposition during the early stage of filtration. Therefore, the steep initial rise in TMP we observed can be attributed to the dramatic hydraulic resistance due to rapid initial particle deposition.

Since this investigation was interested in the resulting pressure due to cake formation, we neglected clean membrane resistance by subtracting ΔP_m, which was measured by the pressure sensor before the syringe pump was started. In Figure 7, ΔP_{cl} is shown, which was associated with the cake area for specific flow rates and filters. It was found that at 300 μL h^{-1}, the 9% porosity filter reached approximately 7.5 kPa (Figure 7a), while the 23% filter reached about 8.0 kPa (Figure 7d) after 300 s. TMP consistently increased with higher flow rate; for example, the final TMP at 500 μL h^{-1} ranged from 16 kPa to 18 kPa, and at 700 μL h^{-1} it ranged from 18.5 kPa to 19.5 kPa across all tested filters.

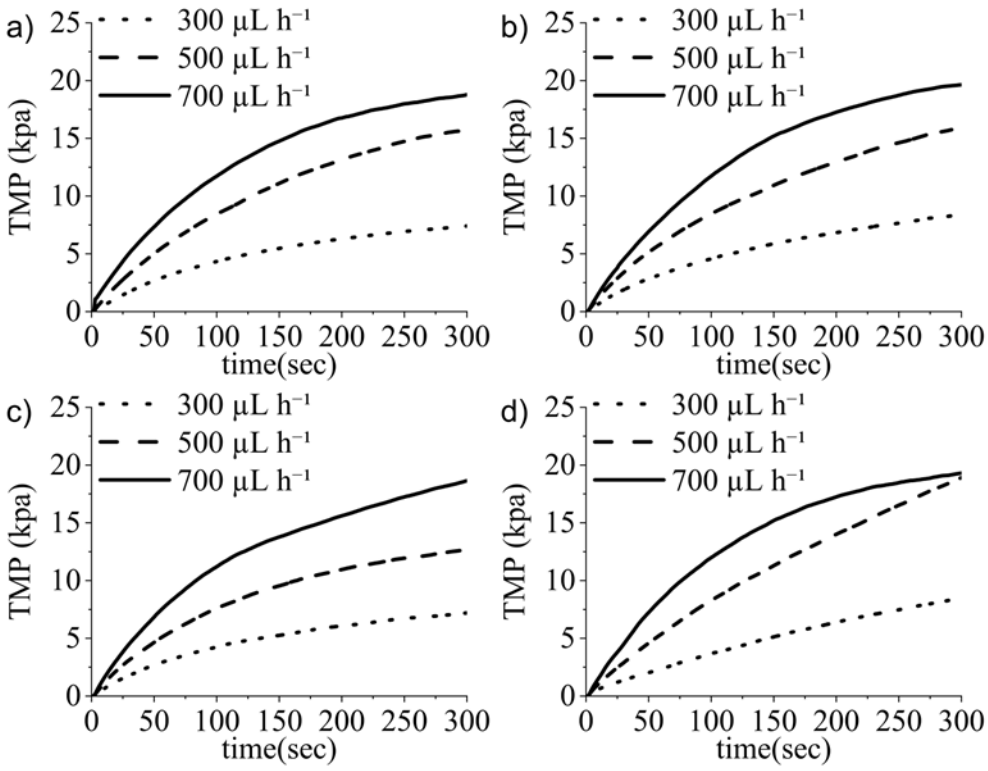


Figure 7. TMP associated with cake area at different flow rates for filters with porosities of (**a**) 9%, (**b**) 12%, (**c**) 17%, and (**d**) 23%.

The observed TMP evolution reflects the combined effects of cake layer growth, internal pore blocking, and cake consolidation. The biphasic pressure profile is observed, where a rapid initial rise is followed by a gradual accumulation. This can be explained by considering the sequential fouling mechanisms that dominate at different stages of the filtration process [62,63]. During the initial phase (0–50 s), particles rapidly deposit on and within the filter membrane. This stage involves simultaneous pore constriction, pore blocking, and the formation of a nascent cake layer [64]. After the initial rapid phase, cake filtration becomes the dominant mechanism. The decelerating pressure rise during this

stage (50–300 s) reflects the transition from rapid cake growth to a regime where cake thickness increases more slowly, and consolidation effects become important [65]. TMP was found to be primarily governed by flow rate rather than filter porosities. For example, after 300 s, the mean TMP across all tested porosities (9–23%) increased from 7.92 ± 0.74 kPa at 300 μL h^{-1} to 19.04 ± 0.26 kPa at 700 μL/h. This flow-rate-dependent TMP increase can be attributed to enhanced particle deposition and bigger cake layer formation at higher flow rates, as discussed earlier. The resulting cake layer contributes additional hydraulic resistance that adds in series with the intrinsic membrane resistance, directly increasing TMP [66]. Multiple linear regression analysis using TMP at 300 s as the dependent variable confirmed that cake area is a statistically significant predictor of TMP ($p = 0.017$), whereas a filter porosity of 9–23% does not exhibit a statistically significant effect ($p > 0.05$ in all cases).

3.3. Cake Porosity

Cake porosity was calculated using Equation (5) over a 300 s filtration period for different flow rates (300, 500, and 700 μL h^{-1}) and filter porosities (9%, 12%, 17%, and 23%). At the lowest flow rate (300 μL h^{-1}), the steady-state porosity in the bulk cake region (beyond 1 mm) stabilized at approximately 0.41–0.44 across all filter types, and the transition zone, where porosity decreased from surface values to bulk values, extended approximately 0.5–1.3 mm into the cake.

As the flow rate increased to 500 μL h^{-1}, bulk cake porosity increased to approximately 0.43–0.46, with the transition zone becoming slightly more extended (0.8–2.1 mm). The most dramatic changes occurred at the highest flow rate (700 μL h^{-1}), where bulk porosity values reached 0.48–0.50, and the transition zone extended to approximately 2.3–2.9 mm, as depicted in Figure 8.

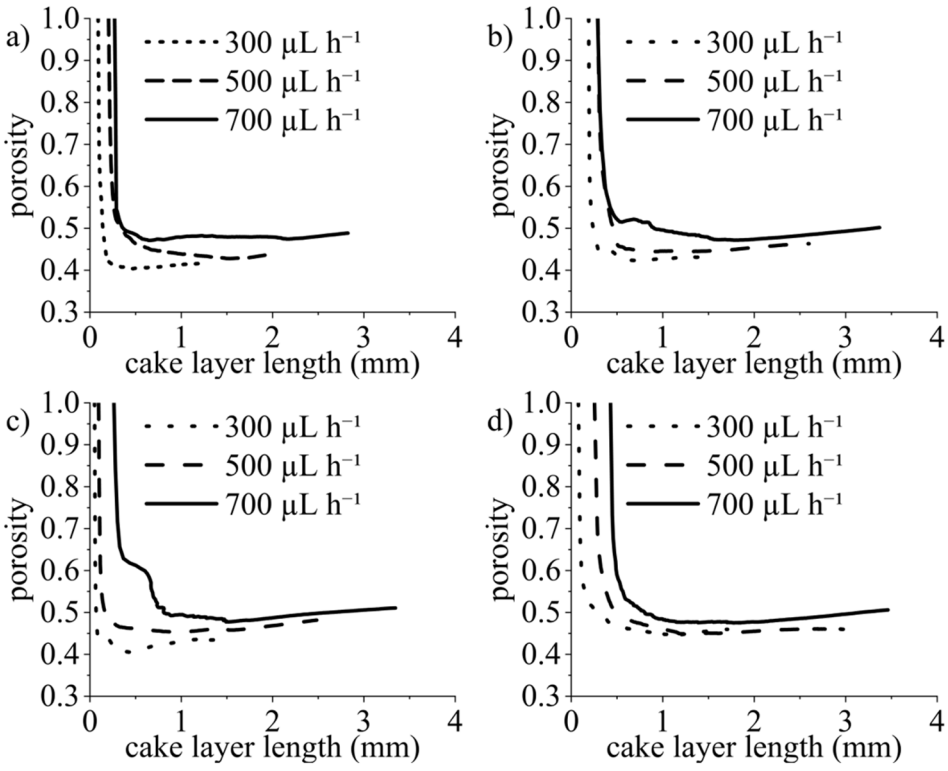


Figure 8. Cake layer porosity over a 300 s period for different filter porosities: the (**a**) 9%, (**b**) 12%, (**c**) 17% and (**d**) 23% porosity filters.

The systematic increase in bulk cake porosity with flow rate (0.41–0.44 at 300 μL h^{-1} versus 0.48–0.50 at 700 μL h^{-1}) reveals that the higher driving force produces less compact

structures. At low flow rates (300 μL h^{-1}), particles arrive at the cake surface slowly, providing a longer interval between successive particle deposition events. For the relatively large 15 μm polystyrene particles used in this study, Brownian translational motion is expected to be weak compared with convective and hydrodynamic transport. Therefore, particle restructuring is more appropriately associated with hydrodynamically and mechanically induced motion, including rolling, sliding, rotation, and local rearrangement along the developing cake surface [67,68]. These processes may allow deposited particles at lower flow rates to relocate toward more mechanically stable and compact configurations before their motion is constrained by subsequently arriving particles.

At high flow rates (700 μL h^{-1}), the rapid particle flux creates a non-equilibrium deposition regime where particles are deposited before achieving optimal packing. The higher particle arrival rate reduces the time available for local rearrangement between successive deposition events, which may kinetically constrain the developing cake structure and result in less efficient packing and a higher void fraction. The extended transition zone (2.3–2.9 mm at 700 μL h^{-1}) suggests that consolidation processes are kinetically limited and cannot keep pace with the rapid cake growth rate.

To confirm the difference in the cake layer structure at different flow rates, we investigated three images from three different flow rates of 12% porous filters. A 1 mm^2 cake area was randomly chosen and investigated using ImageJ software-1.54p. The void space visualization (Figure 9) provides evidence for this mechanism. At 300 μL h^{-1}, the absence of visible voids indicates that particles have achieved dense space-filling arrangements. At 700 μL h^{-1}, the abundant discrete voids represent kinetically trapped non-equilibrium configurations that persist because particle mobility is insufficient to eliminate them once they are buried within the growing cake [69,70].

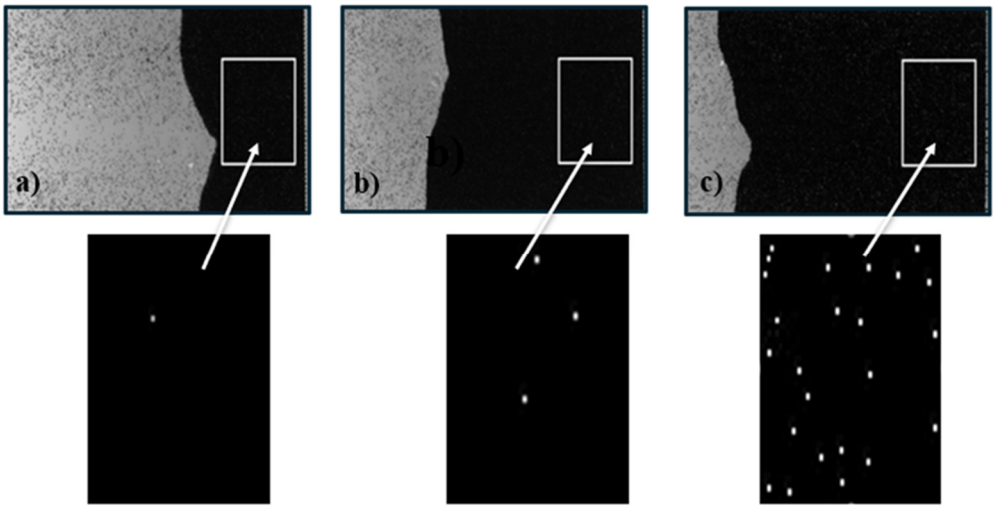


Figure 9. Identified void spaces represented by white spots in a 1 mm^2 cake that formed after 300 s at flow rates of (**a**) 300, (**b**) 500, and (**c**) 700 μL h^{-1}.

4. Conclusions

In this investigation, we fabricated microfilters with porosities that varied from 9% to 23% using photolithography. Microscopic particle image velocimetry (μPIV) experiments were conducted with 1 μm fluorescent seed particles, and the cake layer investigation was carried out with 15 μm polystyrene particles. Experiments were run at three flow rates (300 μL h^{-1}, 500 μL h^{-1}, and 700 μL h^{-1}), and transmembrane pressure (TMP) was continuously monitored using a differential pressure sensor.

In the μPIV analysis, the measured bulk and pore velocities showed excellent agreement with theoretical predictions, and the flow field exhibited strong convergence behavior as fluid approached the 10 μm constriction. In all cases, the streamlines focused on the pore centerline, which intensified at higher flow rates. This velocity acceleration generates substantial hydrodynamic forces that influence particle deposition and cake layer structure. The μPIV results therefore help explain the observed increase in particle deposition, cake growth, and TMP as the flow rate increased. The cake layer experiments showed that cake layer growth was proportional to flow rate, growing from ~3 mm^2 at low flow rates (300 μL h^{-1}) to ~7 mm^2 at the highest flow rates (700 μL h^{-1}). The increased cake area at higher flow rates led to increased hydraulic resistance, raising TMP from 8 kPa to almost 19 kPa.

The TMP profile exhibited biphasic behavior with a sharp initial rise (0–50 s) due to pore blocking and nascent cake formation, followed by a gradual accumulation (50–300 s) from steady cake layer growth. The steady-state porosity of the cake layer ranged from 0.41 to 0.44 at 300 μL h^{-1}, 0.43 to 0.46 at 500 μL h^{-1}, and 0.48 to 0.50 at 700 μL h^{-1}. This implies that at lower flow rates, the particles have enough time to pack into the most space-efficient structures, while at higher flow rates, the high rate of particles being transported to the membrane results in non-equilibrium structures, where the particles are deposited before they have had the chance to pack into the optimal structures. The image analysis of 1 mm^2 cake areas further confirmed this, showing almost no visible voids at 300 μL h^{-1} (dense packing), while abundant discrete voids were observed at 700 μL h^{-1}, representing kinetically trapped configurations.

The quantitative and physical findings in this investigation will assist in developing rational designs of filtration processes, in making informed selections of operating conditions, and in developing predictive engineering models that will accurately represent the interaction of hydrodynamic behavior, particle deposition, and structural development. Moreover, the mechanistic framework developed in this study will assist in optimizing filtration systems for maximum efficiency and reduced fouling.

Supplementary Materials: The following supporting information can be downloaded at: https://www.mdpi.com/article/10.3390/colloids10060077/s1, The data used to generate Figures 4–9.

Author Contributions: Conceptualization, M.G.O. and J.J.J.; methodology, M.G.O. and J.J.J.; software, M.M.U.I. and M.A.K.M.; validation, M.M.U.I. and M.A.K.M.; formal analysis, M.M.U.I. and M.A.K.M.; investigation, M.G.O., J.J.J., M.M.U.I. and M.A.K.M.; resources, M.G.O. and J.J.J.; data curation, M.G.O., J.J.J., M.M.U.I. and M.A.K.M.; writing—original draft preparation, M.M.U.I. and M.A.K.M.; writing—review and editing, M.G.O. and J.J.J.; visualization, M.M.U.I. and M.A.K.M.; supervision, M.G.O. and J.J.J.; project administration, M.G.O. and J.J.J.; funding acquisition, M.G.O. and J.J.J. All authors have read and agreed to the published version of the manuscript.

Funding: This research was funded by the U.S. National Science Foundation, grant numbers 2050105 and 2236466.

Data Availability Statement: The data used to generate Figures 4–9 can be found in the Supplementary Materials.

Conflicts of Interest: The authors declare no conflicts of interest.

Abbreviations

The following abbreviations are used in this manuscript:

TMP	Transmembrane pressure
μPIV	Microscopic particle image velocimetry
PDMS	Polydimethylsiloxane

References

1. Edd, J.F.; Mishra, A.; Dubash, T.D.; Herrera, S.; Mohammad, R.; Williams, E.K.; Hong, X.; Mutlu, B.R.; Walsh, J.R.; de Carvalho, F.M.; et al. Microfluidic Concentration and Separation of Circulating Tumor Cell Clusters from Large Blood Volumes. *Lab Chip* **2020**, *20*, 558–567. [CrossRef] [PubMed]
2. Wang, Y.; Keller, K.; Cheng, X. Tangential Flow Microfiltration for Viral Separation and Concentration. *Micromachines* **2019**, *10*, 320. [CrossRef] [PubMed]
3. Chernyshev, V.S.; Yashchenok, A.; Ivanov, M.; Silachev, D.N. Filtration-Based Technologies for Isolation, Purification and Analysis of Extracellular Vesicles. *Phys. Chem. Chem. Phys.* **2023**, *25*, 23344–23357. [CrossRef] [PubMed]
4. Li, H.; Raza, A.; Yuan, S.; AlMarzooqi, F.; Fang, N.X.; Zhang, T. Biomimetic On-Chip Filtration Enabled by Direct Micro-3D Printing on Membrane. *Sci. Rep.* **2022**, *12*, 8178. [CrossRef] [PubMed]
5. Samari-Kermani, M.; de Vries, E.T.; Schijven, J.F.; Raoof, A. A Closer Look at the Role of Biofilms in Water Filtration: Bridging Microscopic Insights with System Performance. *J. Water Process Eng.* **2024**, *67*, 106104. [CrossRef]
6. Qasim, M.; Duong, D.D.; Lee, J.Y.; Lee, N.Y. Fabrication of Polycaprolactone Nanofibrous Membrane-Embedded Microfluidic Device for Water Filtration. *J. Appl. Polym. Sci.* **2020**, *137*, 49207. [CrossRef]
7. Bergua, J.F.; Hu, L.; Fuentes-Chust, C.; Álvarez-Diduk, R.; Hassan, A.H.A.; Parolo, C.; Merkoçi, A. Lateral Flow Device for Water Fecal Pollution Assessment: From Troubleshooting of Its Microfluidics Using Bioluminescence to Colorimetric Monitoring of Generic *Escherichia coli*. *Lab Chip* **2021**, *21*, 2417–2426. [CrossRef] [PubMed]
8. Mesquita, P.; Gong, L.; Lin, Y. A Low-Cost Microfluidic Method for Microplastics Identification: Towards Continuous Recognition. *Micromachines* **2022**, *13*, 499. [CrossRef] [PubMed]
9. Park, W.; Lee, J.; Kim, M. Recent Progress of Inertial Microfluidics for High-Throughput and Scalable Separation of Microscale Bioparticles. *Sens. Actuators A Phys.* **2025**, *382*, 116112. [CrossRef]
10. Wang, S.; Xu, Q.; Cai, Y.; Wang, Q.; Liu, Y.; Wang, D. Biological Particle Separation Techniques Based on Microfluidics. *Interdiscip. Med.* **2024**, *2*, e20240003. [CrossRef]
11. Hasan, M.S.; Marsafari, M.; Tolosa, M.; Andar, A.; Ramamurthy, S.S.; Ge, X.; Kostov, Y.; Rao, G. Rapid Ultrasensitive and High-Throughput Bioburden Detection: Microfluidics and Instrumentation. *Anal. Chem.* **2022**, *94*, 8683–8692. [CrossRef] [PubMed]
12. Chen, X.; Shen, J. Review of Membranes in Microfluidics. *J. Chem. Technol. Biotechnol.* **2017**, *92*, 271–282. [CrossRef]
13. Bouhid de Aguiar, I.; Schroën, K. Microfluidics Used as a Tool to Understand and Optimize Membrane Filtration Processes. *Membranes* **2020**, *10*, 316. [CrossRef] [PubMed]
14. Chen, X.; Shen, J.; Hu, Z.; Huo, X. Manufacturing Methods and Applications of Membranes in Microfluidics. *Biomed. Microdevices* **2016**, *18*, 104. [CrossRef] [PubMed]
15. Mohammadimehr, A.; Rodríguez-Villarreal, A.I.; López Martínez, J.A.; Casals-Terré, J. Review: Impact of Microfluidic Cell and Particle Separation Techniques on Microplastic Removal Strategies. *J. Agric. Food Res.* **2024**, *16*, 101124. [CrossRef]
16. Islam, M.M.U. Numerical Analysis of Particle Sorting by Acoustic Waves in Microfluidics. *BAUET J.* **2024**, *4*, 17–21. [CrossRef]
17. Ismail, A.F.; Goh, P.S. Microfiltration Membrane. In *Encyclopedia of Polymeric Nanomaterials*; Kobayashi, S., Müllen, K., Eds.; Springer: Berlin/Heidelberg, Germany, 2015; pp. 1250–1255, ISBN 978-3-642-29648-2.
18. Bouhid De Aguiar, I.; Meireles, M.; Bouchoux, A.; Schroën, K. Microfluidic Model Systems Used to Emulate Processes Occurring during Soft Particle Filtration. *Sci. Rep.* **2019**, *9*, 3063. [CrossRef] [PubMed]
19. Dressaire, E.; Sauret, A. Clogging of Microfluidic Systems. *Soft Matter* **2017**, *13*, 37–48. [CrossRef] [PubMed]
20. Liu, Y.; Wang, Z.; Xu, M.; Qi, F.; Li, C.; Sun, D.; Nan, J.; Li, W.; Guan, X.; Ikhlaq, A. Unveiling the Role of Cake Layer in Coagulation-Ultrafiltration on Membrane Fouling and Emerging Application as Dynamic Membrane before Ultrafiltration. *Sep. Purif. Technol.* **2024**, *350*, 127932. [CrossRef]
21. Mokrane, M.L.; Desclaux, T.; Morris, J.F.; Joseph, P.; Liot, O. Microstructure of the Near-Wall Layer of Filtration-Induced Colloidal Assembly. *Soft Matter* **2020**, *16*, 9726–9737. [CrossRef] [PubMed]
22. Bacchin, P.; Marty, A.; Duru, P.; Meireles, M.; Aimar, P. Colloidal Surface Interactions and Membrane Fouling: Investigations at Pore Scale. *Adv. Colloid Interface Sci.* **2011**, *164*, 2–11. [CrossRef] [PubMed]
23. Valencia, A.; Le Men, C.; Ellero, C.; Lafforgue-Baldas, C.; Schmitz, P.; Morris, J.F. Direct Observation at the Microscale of Particle Deposition during the First Stage of the Microfiltration Process. *J. Membr. Sci.* **2020**, *599*, 117823. [CrossRef]
24. Sorrentino, G.; Gajjar, P.; Withers, P.J.; Chellappah, K.; Biscontin, G. Experimental Investigation of Filter Cake Deposition under Cross-Flow and Static Filtration Conditions. *Chem. Eng. Sci.* **2024**, *283*, 119417. [CrossRef]
25. Altmann, J.; Ripperger, S. Particle Deposition and Layer Formation at the Crossflow Microfiltration. *J. Membr. Sci.* **1997**, *124*, 119–128. [CrossRef]
26. Ozofor, I.H.; Tarabara, V.V.; Da Costa, A.R.; Morse, A.N. Analysis of Microstructural Properties of Ultrafiltration Cake Layer during Its Early Stage Formation and Growth. *J. Membr. Sci.* **2021**, *620*, 118903. [CrossRef]

27. Valencia, A.; LeMen, C.; Ellero, C.; Lafforgue-Baldas, C.; Morris, J.F.; Schmitz, P. Direct Observation of the Microfiltration of Yeast Cells at the Micro-Scale: Characterization of Cake Properties. *Sep. Purif. Technol.* **2022**, *298*, 121614. [CrossRef]
28. Lüken, A.; Linkhorst, J.; Fröhlingsdorf, R.; Lippert, L.; Rommel, D.; De Laporte, L.; Wessling, M. Unravelling Colloid Filter Cake Motions in Membrane Cleaning Procedures. *Sci. Rep.* **2020**, *10*, 20043. [CrossRef] [PubMed]
29. Islam, M.M.U.; Olsen, M.G.; Juárez, J.J. Acoustic Mitigation of Cake Formation in Microfluidic Membrane Filtration. *Colloid Interface Sci. Commun.* **2026**, *73*, 100905. [CrossRef]
30. Bräsel, B.; Yoo, S.-W.; Huber, S.; Wessling, M.; Linkhorst, J. Evolution of Particle Deposits at Communicating Membrane Pores during Crossflow Filtration. *J. Membr. Sci.* **2023**, *686*, 121977. [CrossRef]
31. Song, S.; Le-Clech, P.; Shen, Y. Microscale Fluid and Particle Dynamics in Filtration Processes in Water Treatment: A Review. *Water Res.* **2023**, *233*, 119746. [CrossRef] [PubMed]
32. Gu, B.; Sanaei, P.; Kondic, L.; Cummings, L.J. *Stochastic Modeling of Filtration with Sieving in Graded Pore Networks*; Cambridge University Press: Cambridge, UK, 2025.
33. Lüken, A.; Stüwe, L.; Lohaus, J.; Linkhorst, J.; Wessling, M. Particle Movements Provoke Avalanche-like Compaction in Soft Colloid Filter Cakes. *Sci. Rep.* **2021**, *11*, 12836. [CrossRef] [PubMed]
34. Jiang, S.; Chatterjee, S.G. A Surface-renewal Model for Constant Flux Cross-flow Microfiltration. *J. Appl. Polym. Sci.* **2015**, *132*, 41778. [CrossRef]
35. Islam, M.U. Evolution of Cake Formation and Pressure Dynamics in Porous Microfluidic Filters. Master's Thesis, Iowa State University, Ames, IA, USA, 2025.
36. Fox, R.W.; McDonald, A.T. *Introduction to Fluid Mechanics*, 5th ed.; J. Wiley: New York, NY, USA, 1998; ISBN 0-471-12464-8.
37. Raffel, M.; Willert, C.E.; Wereley, S.T.; Kompenhans, J. *Particle Image Velocimetry: A Practical Guide*; Springer: Berlin/Heidelberg, Germany, 2007; ISBN 978-3-540-72307-3.
38. Bakhtiari, A.; Kähler, C.J. Enhanced Particle Separation through Ultrasonically-Induced Microbubble Streaming for Automated Size-Selective Particle Depletion. *RSC Adv.* **2024**, *14*, 2226–2234. [CrossRef] [PubMed]
39. Thielicke, W.; Stamhuis, E.J. PIVlab—Towards User-Friendly, Affordable and Accurate Digital Particle Image Velocimetry in MATLAB. *J. Open Res. Softw.* **2014**, *2*, e30. [CrossRef]
40. Miah, M.A.K.; Islam, M.M.U.; Ghosh, R.; Tangudu, C.; Olsen, M.G.; Juárez, J.J. Acoustic Streaming Micromixer with Embedded Obstacle Arrays for Dispersion Enhancement. *Heat Mass Transf.* **2026**, *62*, 129. [CrossRef]
41. Olsen, M.G.; Adrian, R.J. Out-of-Focus Effects on Particle Image Visibility and Correlation in Microscopic Particle Image Velocimetry. *Exp. Fluids* **2000**, *29*, S166–S174. [CrossRef]
42. Bourdon, C.J.; Olsen, M.G.; Gorby, A.D. The Depth of Correlation in Micro-PIV for High Numerical Aperture and Immersion Objectives. *J. Fluids Eng.* **2006**, *128*, 883–886. [CrossRef]
43. Bourdon, C.J.; Olsen, M.G.; Gorby, A.D. Power-Filter Technique for Modifying Depth of Correlation in microPIV Experiments. *Exp. Fluids* **2004**, *37*, 263–271. [CrossRef]
44. Bourdon, C.J.; Olsen, M.G.; Gorby, A.D. Validation of an Analytical Solution for Depth of Correlation in Microscopic Particle Image Velocimetry. *Meas. Sci. Technol.* **2004**, *15*, 318–327. [CrossRef]
45. Miele, F.; De Anna, P.; Dentz, M. Stochastic Model for Filtration by Porous Materials. *Phys. Rev. Fluids* **2019**, *4*, 094101. [CrossRef]
46. Cheng, Y.-H.; Tsai, C.-J. Factors Influencing Pressure Drop through a Dust Cake during Filtration. *Aerosol Sci. Technol.* **1998**, *29*, 315–328. [CrossRef]
47. Kim, D.; Chesler, N.C.; Beebe, D.J. A Method for Dynamic System Characterization Using Hydraulic Series Resistance. *Lab Chip* **2006**, *6*, 639–644. [CrossRef] [PubMed]
48. Panigrahi, P.K. *Transport Phenomena in Microfluidic Systems*, 1st ed.; Wiley: Singapore, 2016; ISBN 978-1-118-29841-1.
49. Batchelor, G.K. *An Introduction to Fluid Dynamics*, 1st ed.; Cambridge University Press: Cambridge, UK, 2000; ISBN 978-0-521-66396-0.
50. Cheng, N.-S. Formula for the Viscosity of a Glycerol−Water Mixture. *Ind. Eng. Chem. Res.* **2008**, *47*, 3285–3288. [CrossRef]
51. Bear, J. Dynamics of Fluids in Porous Media. *Soil Sci.* **1975**, *120*, 162–163. [CrossRef]
52. Holdich, R. *Fundamentals of Particle Technology*; MidlandIT: Leicestershire, UK, 2020; ISBN 0-9543881-2-7.
53. Wereley, S.T.; Meinhart, C.D. Recent Advances in Micro-Particle Image Velocimetry. *Annu. Rev. Fluid Mech.* **2010**, *42*, 557–576. [CrossRef]
54. Santiago, J.G.; Wereley, S.T.; Meinhart, C.D.; Beebe, D.J.; Adrian, R.J. A Particle Image Velocimetry System for Microfluidics. *Exp. Fluids* **1998**, *25*, 316–319. [CrossRef]
55. Barbosa, F.; Dueñas-Pamplona, J.; Abreu, C.S.; Oliveira, M.S.N.; Lima, R.A. Numerical Model Validation of the Blood Flow through a Microchannel Hyperbolic Contraction. *Micromachines* **2023**, *14*, 1886. [CrossRef] [PubMed]
56. Meinhart, C.D.; Wereley, S.T.; Santiago, J.G. PIV Measurements of a Microchannel Flow. *Exp. Fluids* **1999**, *27*, 414–419. [CrossRef]
57. Oliveira, M.S.N.; Alves, M.A.; Pinho, F.T.; McKinley, G.H. Viscous Flow through Microfabricated Hyperbolic Contractions. *Exp. Fluids* **2007**, *43*, 437–451. [CrossRef]

58. Jiang, D.; Ni, C.; Tang, W.; Huang, D.; Xiang, N. Inertial Microfluidics in Contraction–Expansion Microchannels: A Review. *Biomicrofluidics* **2021**, *15*, 041501. [CrossRef] [PubMed]
59. Henry, C.; Minier, J.-P.; Lefèvre, G. Towards a Description of Particulate Fouling: From Single Particle Deposition to Clogging. *Adv. Colloid Interface Sci.* **2012**, *185–186*, 34–76. [CrossRef] [PubMed]
60. Geankoplis, C.J. *Transport Processes and Unit Operations*; Pearson College Div: Engelwood Cliffs, NJ, USA, 1993; ISBN 978-0-13-930439-2.
61. Jönsson, A.-S.; Jönsson, B. Ultrafiltration of Colloidal Dispersions—A Theoretical Model of the Concentration Polarization Phenomena. *J. Colloid Interface Sci.* **1996**, *180*, 504–518. [CrossRef]
62. Ho, C.-C.; Zydney, A.L. A Combined Pore Blockage and Cake Filtration Model for Protein Fouling during Microfiltration. *J. Colloid Interface Sci.* **2000**, *232*, 389–399. [CrossRef] [PubMed]
63. Bolton, G.; Lacasse, D.; Kuriyel, R. Combined Models of Membrane Fouling: Development and Application to Microfiltration and Ultrafiltration of Biological Fluids. *J. Membr. Sci.* **2006**, *277*, 75–84. [CrossRef]
64. Duclos-Orsello, C.; Li, W.; Ho, C.-C. A Three Mechanism Model to Describe Fouling of Microfiltration Membranes. *J. Membr. Sci.* **2006**, *280*, 856–866. [CrossRef]
65. Tien, C.; Bai, R.; Ramarao, B.V. Analysis of Cake Growth in Cake Filtration: Effect of Fine Particle Retention. *AIChE J.* **1997**, *43*, 33–44. [CrossRef]
66. Ohanessian, K.; Monnot, M.; Moulin, P.; Ferrasse, J.-H.; Barca, C.; Soric, A.; Boutin, O. Dead-End and Crossflow Ultrafiltration Process Modelling: Application on Chemical Mechanical Polishing Wastewaters. *Chem. Eng. Res. Des.* **2020**, *158*, 164–176. Erratum in *Chem. Eng. Res. Des.* **2020**, *162*, 38. [CrossRef]
67. Hubbe, M.A. Theory of Detachment of Colloidal Particles from Flat Surfaces Exposed to Flow. *Colloids Surf.* **1984**, *12*, 151–178. [CrossRef]
68. Li, H.; Fane, A.G.; Coster, H.G.L.; Vigneswaran, S. Direct Observation of Particle Deposition on the Membrane Surface during Crossflow Microfiltration. *J. Membr. Sci.* **1998**, *149*, 83–97. [CrossRef]
69. Dersoir, B.; De Saint Vincent, M.R.; Abkarian, M.; Tabuteau, H. Clogging of a Single Pore by Colloidal Particles. *Microfluid Nanofluid* **2015**, *19*, 953–961. [CrossRef]
70. O'Hern, C.S.; Silbert, L.E.; Liu, A.J.; Nagel, S.R. Jamming at Zero Temperature and Zero Applied Stress: The Epitome of Disorder. *Phys. Rev. E* **2003**, *68*, 011306. [CrossRef] [PubMed]

Disclaimer/Publisher's Note: The statements, opinions and data contained in all publications are solely those of the individual author(s) and contributor(s) and not of MDPI and/or the editor(s). MDPI and/or the editor(s) disclaim responsibility for any injury to people or property resulting from any ideas, methods, instructions or products referred to in the content.